

# Synoptic Solar Cycle 24 in Corona, Chromosphere, and Photosphere Seen by the *Solar Dynamics Observatory*

E. Benevolenskaya · G. Slater · J. Lemen

Received: 17 October 2013 / Accepted: 5 April 2014 / Published online: 30 April 2014  
© Springer Science+Business Media Dordrecht 2014

**Abstract** The *Solar Dynamics Observatory* provides multiwavelength imagery from extreme ultraviolet (EUV) to visible light as well as magnetic-field measurements. These data enable us to study the nature of solar activity in different regions of the Sun, from the interior to the corona. For solar-cycle studies, synoptic maps provide a useful way to represent global activity and evolution by extracting a central meridian band from sequences of full-disk images over a full solar Carrington rotation ( $\approx 27.3$  days). We present the global evolution during Solar Cycle 24 from 20 May 2010 to 31 August 2013 (CR 2097–CR 2140), using synoptic maps constructed from full-disk, line-of-sight magnetic-field imagery and EUV imagery (171 Å, 193 Å, 211 Å, 304 Å, and 335 Å). The synoptic maps have a resolution of 0.1 degree in longitude and steps of 0.001 in sine of latitude. We studied the axisymmetric and non-axisymmetric structures of solar activity using these synoptic maps. To visualize the axisymmetric development of Cycle 24, we generated time–latitude (also called butterfly) images of the solar cycle in all of the wavelengths, by averaging each synoptic map over all longitudes, thus compressing it to a single vertical strip, and then assembling these strips in time order. From these time–latitude images we observe that during the ascending phase of Cycle 24 there is a very good relationship between the integrated magnetic flux and the EUV intensity inside the zone of sunspot activities. We observe a North–South asymmetry

---

The Many Scales of Solar Activity in Solar Cycle 24 as seen by SDO  
Guest Editors: Aaron Birch, Mark Cheung, Andrew Jones, and W. Dean Pesnell

---

E. Benevolenskaya (✉)  
Pulkovo Astronomical Observatory, St. Petersburg, 196140, Russia  
e-mail: [benevolenskayae@mail.ru](mailto:benevolenskayae@mail.ru)

E. Benevolenskaya  
St. Petersburg State University, St. Petersburg, 198504, Russia

G. Slater · J. Lemen  
Lockheed Martin Lab, Palo Alto, CA 94303, USA

G. Slater  
e-mail: [slater@lmsal.com](mailto:slater@lmsal.com)

J. Lemen  
e-mail: [lemen@lmsal.com](mailto:lemen@lmsal.com)

of the EUV intensity in high-latitudes. The North–South asymmetry of the emerging magnetic flux developed and resulted in a consequential asymmetry in the timing of the polar magnetic-field reversals.

**Keywords** Solar cycle, observations · Magnetic fields, photosphere · Magnetic fields, corona

## 1. Introduction

The behavior of the current solar cycle, Cycle 24, is of great interest because this cycle follows a long and deep solar minimum in Cycle 23. Moreover, the predictions of sunspot number for Cycle 24 at solar maximum vary widely: from 40 to 185 (Pesnell, 2012).

This circumstance has encouraged researchers to study the evolution of solar activity during this period and compare it with simulations of the solar dynamo (Spruit, 2012). Petrie (2012) has analyzed the ascending phase of Cycle 24 and compared it with the corresponding phase of previous cycles using magnetograph data from the National Solar Observatory/Kitt Peak and Mount Wilson Observatory. Using 37 years of full-disk observations from Kitt Peak and Mt. Wilson magnetographs covering several solar cycles, statistically significant patterns were found that are consistent with the Babcock–Leighton phenomenological model for the solar cycle (Petrie, 2012). To reconcile the visible behavior of solar activity with the various transport models, Jiang *et al.* (2013) found it necessary to take into account the fluctuations of meridional flows and the tilts of active regions. However, sometimes the simulation of magnetic-flux transport leads to ambiguous conclusions that challenge the transport models themselves. Using observations from the *Hinode* spacecraft during the period 2008–2012, a delay was discovered in the timing of the decrease of old magnetic flux near the south heliographic pole as compared with the corresponding timing of the decrease of the north polar magnetic field. This observation presents a difficulty for the theory of the solar cycle (Shiota *et al.*, 2012). On the other hand, Svalgaard and Kamide (2012) suggested that the North–South asymmetry of polar magnetic fields may be the result of the asymmetry in the appearance of magnetic flux in the active-region belts. Therefore, investigating the detailed evolution of the solar activity in the photosphere, corona, and chromosphere is quite important for understanding the solar-cycle evolution.

In this article we have analyzed data from the *Solar Dynamics Observatory* (SDO: Pesnell, Thompson, and Chamberlin, 2012) to investigate the relationship between the evolution of magnetic activity in the photosphere and corona during the ascending phase of Cycle 24 and the nature of the observed delay in the reversals of the polar magnetic fields.

## 2. Observations

The *Atmospheric Imaging Assembly* (AIA: Lemen *et al.*, 2012) onboard SDO provides continuous, nearly simultaneous, high-resolution full-disk images of the corona and the transition region with 12-second temporal cadence. AIA consists of four telescopes that employ normal-incidence, multilayer-coated optics to provide narrow-band imaging of seven extreme ultraviolet (EUV) band passes centered on specific lines: Fe XVIII (94 Å), Fe VIII and XXI (131 Å), Fe IX (171 Å), Fe XII, XXIV (193 Å), Fe XIV (211 Å), He II (304 Å), and Fe XVI (335 Å). One telescope observes C IV (near 1600 Å) and the nearby continuum (1700 Å) and has a filter that observes in the visible to enable co-alignment with images

from other telescopes. The temperature diagnostics of the EUV emissions cover the range from  $6 \times 10^4$  K to  $2 \times 10^7$  K (Lemen *et al.*, 2012). Coronal holes (regions of low density), EUV bright points, and coronal loops are well-defined in the 193 Å channel because of the existence of two temperature peaks at  $\log T = 6.1$  and  $\log T = 7.3$ . The quiet corona and upper transition region (up to 1 MK) are seen in the 171 Å channel. The active-region corona is imaged in the 211 Å and the 335 Å channels, which have slightly different temperature peaks ( $\log T = 6.3$  and  $\log T = 6.4$ ). The low-temperature chromosphere and transition region (about 0.05 MK) are observed in the 304 Å channel. The *Helioseismic and Magnetic Imager* (HMI; Scherrer *et al.*, 2012) instrument is an enhanced version of the *Michelson Doppler Imager* (MDI; Scherrer *et al.*, 1995) instrument, which is part of the *Solar and Heliospheric Observatory* (SOHO)

HMI provides full-disk images every 45 seconds for the line-of-sight (LOS) component of the magnetic-field strength. HMI has 0.5 arcsecond pixels and or 1 arcsec spatial resolution. AIA has 0.6 arcsecond pixels, and the EUV channels have 1.5 arcsec spatial resolution.

### 3. Data Analysis and Results

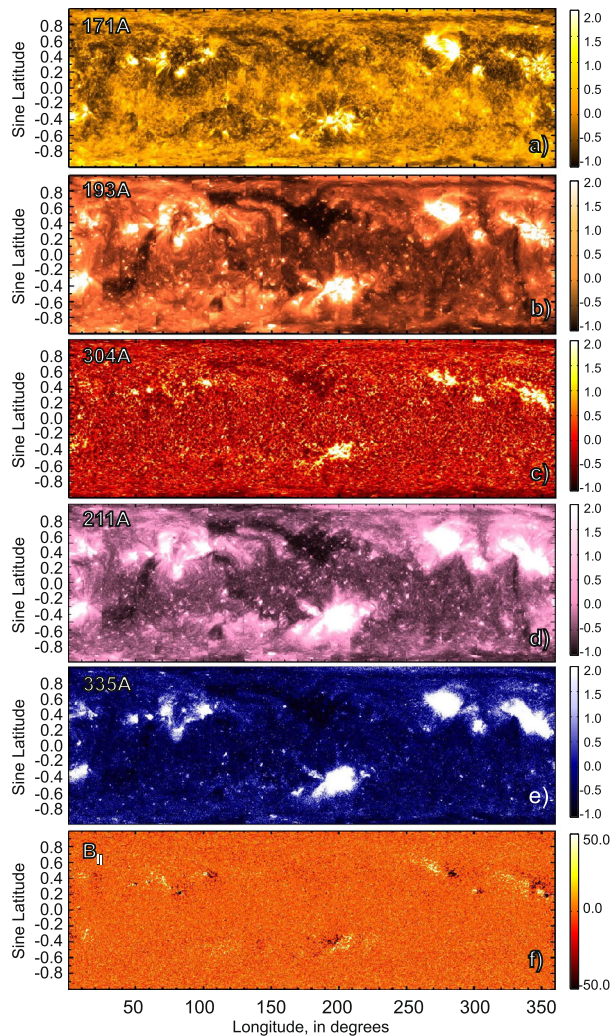
The daily full-disk EUV images are re-mapped to a high-resolution Carrington coordinate grid, resulting in a synoptic frame. The synoptic maps are constructed by combining central meridian strips of 15-degree width in longitude from each synoptic frame. The longitudinal pixel of these maps is  $0.1^\circ$  (3600 points from  $0.1^\circ$  to  $360^\circ$ ). The latitudinal pixel is 0.001 of sine latitude per pixel from  $-1.0$  to  $1.0$ . The EUV synoptic maps are normalized as follows: the value of EUV emission [ $I(i, j)$ ] in the  $(i, j)$  pixel of the synoptic map is divided by the value of EUV emission averaged over all pixels:  $I_{\text{norm}}(i, j) = (I(i, j) - I)/I$ .

We have constructed normalized EUV synoptic maps for the AIA EUV channels 171 Å, 193 Å, 211 Å, 304 Å and 335 Å for Carrington rotations CR 2097–CR 2140 (20 May 2010–31 August 2013). Example maps for CR 2100 (9 August 2010–5 October 2010) are shown in Figure 1. For comparison, the LOS magnetic-field synoptic map is shown in panel f. There is a good relationship between the activity regions visible in the EUV emission with the regions of strong magnetic field. Each EUV bright region is associated with a complex of solar activity. During this particular Carrington rotation the complexes of solar activity show a longitudinally non-uniform distribution. Moreover, there exists a North–South asymmetry (northern hemisphere is more active). In addition, in the North, there is a coronal hole visible as a dark region in the maps for 193 Å and 304 Å within the range of  $150^\circ$ – $200^\circ$  in longitude. The 304 Å emission is mainly chromosphere in origin, so the 304 Å maps clearly show the chromospheric network (Figure 1c).

In Figure 2, panels b and c, stack-plots of smoothed EUV 193 Å and LOS synoptic maps show non-axisymmetric or longitudinally non-uniform structures for the ascending phase of Solar Cycle 24 from 20 May 2010 to 31 August 2013. The sunspot number is plotted in panel a. The development of magnetic activity is associated with the changing topology of the corona. Note that during the time interval spanned by Carrington rotations CR 2116–CR 2119 (first sunspot maximum) there is a persistent, extended coronal hole in the southern hemisphere. This sunspot maximum coincides with the sunspot maximum in the northern hemisphere as well as with the weak activity in the southern hemisphere.

We also studied the axisymmetric behavior of solar activity in EUV lines. For this purpose each normalized synoptic map was averaged over all longitudes to produce a butterfly diagram in sine latitude–time coordinates (Figure 3, panels e, f, g, and h). For comparison, the total magnetic flux [ $|B_{\parallel}|$ ] is shown in panel d and the LOS field [ $B_{\parallel}$ ] is shown in panel c.

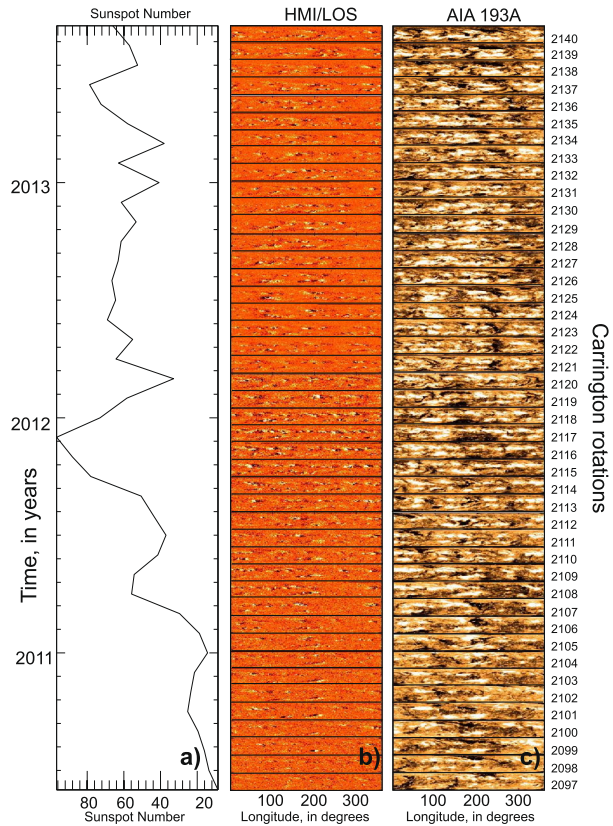
**Figure 1** Normalized synoptic maps of the EUV emission of lines in relative units  $[-1, 2]$ : (a) 171 Å; (b) 193 Å; (c) 304 Å; (d) 211 Å; (e) 335 Å; and (f) line-of-sight component of the magnetic-field strength,  $[-50 \text{ G}, 50 \text{ G}]$ , for Carrington rotation CR 2100 (9 August 2010–5 September 2010)



The total sunspot area, interpolated in time intervals referenced to the Carrington rotation, is plotted in Figure 2, panel a. The total magnetic flux inside the sunspot-activity latitudinal zones  $[0^\circ - 40^\circ \text{ N, S}]$  is shown in panel b. Variations of the sunspot area agree with the emerged magnetic flux inside the sunspot-activity zones for both hemispheres (Figure 3, panels a and b). In Figure 3, panel d, the total magnetic flux can be seen to be composed of impulses of solar activity corresponding to emerged magnetic flux. During the solar cycle the mean latitude of this emerged magnetic flux moves toward the Equator (Spörer's law). There is a North–South asymmetry in the emerged magnetic flux. In the North, the emerged magnetic flux reached its maximum value in November 2011, while in South the maximum occurred in July 2012.

In Cycle 24 the picture of magnetic activity is more complicated than in Solar Cycle 23 (Benevolenskaya, Kosovichev, and Scherrer, 2001; Benevolenskaya *et al.*, 2002) because of the occurrence of a strong fluctuation or surge of negative (old cycle) polarity above latitude  $30^\circ$  in 2011 (Figure 3, annotation A) in the northern hemisphere, while in the southern

**Figure 2** (a) Monthly sunspot number from 20 May 2010 to 31 August 2013; (b) HMI synoptic maps [ $-25$  G,  $25$  G] from CR 2097 to CR 2140; (c) AIA EUV synoptic maps for the same Carrington rotations as (b) in the Fe XII, XXIV  $193$  Å channel.



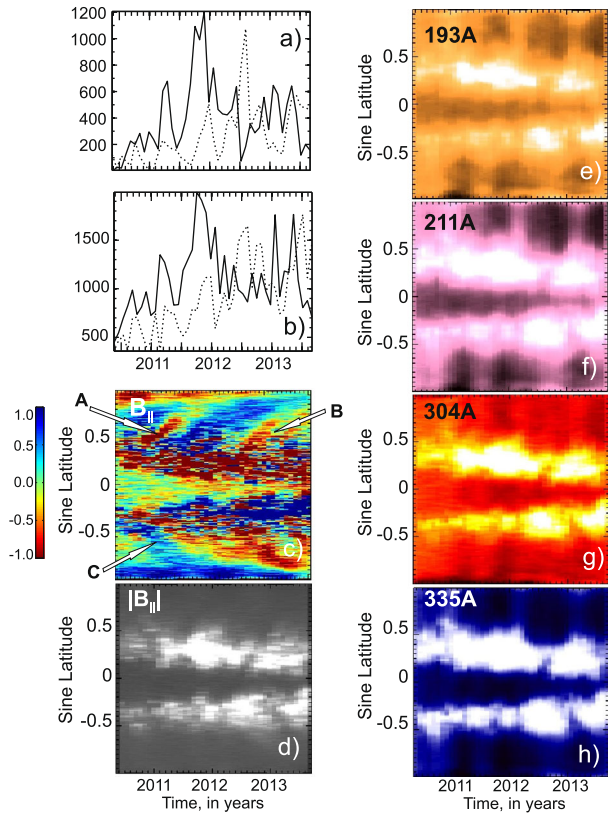
hemisphere, a positive (old cycle) fluctuation began in 2010 (Figure 3, annotation C), which similarly delays the polar magnetic-field reversal. The next strong fluctuation of negative polarity in the northern hemisphere (Figure 3, annotation B) occurred in 2012–2013 during the ascending phase of Cycle 24. We denote the old-cycle polarity as a polarity of the polar magnetic field before the reversals.

According to the classical transport models, the zones of alternative polarities (a positive and a negative) of the emerged magnetic flux, which are visible as so-called surges in Figure 3d, spread from mid- to high latitudes under the influence of turbulent diffusion, differential rotation, and meridional circulation (Wang, Nash, and Sheeley, 1989). Owing to Joy's law and Hale's law, the trailing portions of active regions are statistically more likely to be carried poleward than are the leading portions. This process drives the polarity reversal of the polar magnetic field. The statistical tilt of emerging magnetic flux forms two latitudinal rings of flux of opposite polarity in the active-latitude zones in each hemisphere for each emerging bi-polar complex of solar activity. In reality, this leads to multiband patterns in latitude because of numerous emerging solar complexes, as seen in the LOS axisymmetric distribution within the activity zones. However, the statistical variability of active-region tilts may lead to variations of this scenario. This can create situations in which the leading portions of emerging active regions extend to higher latitudes than trailing portions.

The scatter plots of the summarized EUV emissions (normalized values) and the integrated magnetic flux at latitudes from  $-35^\circ$  to  $35^\circ$  obtained from the axisymmetrical dis-

**Figure 3** Axisymmetrical pattern of Solar Cycle 24 from 20 May 2010 to 31 August 2013.

(a) The interpolated sunspot area with a reference to the beginning of the Carrington rotation for northern (solid line) and for southern (dashed lines) hemispheres; (b) Magnetic flux in sunspot-activity latitudinal zone from  $0^\circ$  to  $40^\circ$  for northern (solid line) and southern (dashed lines) hemispheres as a sum of  $|B_{||}|$ ; (c) Line-of-sight component of the magnetic-field strength  $[B_{||}, (-1 \text{ G}, 1 \text{ G})]$ , filtering by  $3 \times 3$  pixels, red is negative polarity, blue is positive polarity; (d) Magnetic flux as  $|B_{||}|$ , [0 20 G]; (e) 193 Å; (f) 211 Å; (g) 304 Å; (h) 335 Å. All images have been smoothed using a  $3 \times 3$ -pixel average.



tributions are represented in Figure 4. The EUV intensity and the integrated magnetic flux are strongly correlated in the axisymmetrical distributions. The correlation coefficients for lines EUV 193 Å, EUV 171 Å, EUV 304 Å, and EUV 335 Å are 0.95, 0.65, 0.97, and 0.89. The lowest value corresponds to the emission of line EUV 171 Å, which comes from the quiet corona and upper transition region. The He II lines (304 Å) come from chromosphere and transition region and show the highest relationship between the magnetic flux and EUV intensity in sunspot-activity zones. Therefore, the increase of the magnetic flux leads to the increase of the EUV intensity, and the butterfly diagram of the EUV emissions follows the distributions of the magnetic flux at latitudes of sunspot-activity zones (Figure 3). To illustrate the high-latitude distributions of the EUV emissions, we have constructed plots of mean EUV intensity for line 171 Å as a function of latitudes from  $53^\circ$  to  $90^\circ$  in the northern and southern hemispheres, respectively. All represented data are averaged over Carrington rotations: CR 2097–CR 2101, CR 2102–CR 2106, CR 2107–CR 2111, CR 2112–CR 2116, CR 2117–CR 2121, CR 2122–CR 2126, CR 2127–CR 2131, CR 2132–CR 2136, and CR 2137–CR 2140 (Figure 5). In the South we observe a maximum of the EUV emission in line 171 Å at latitudes of around  $-60^\circ$ . With time, this maximum shifts to higher latitudes. In the North the peak of the EUV emission occurs within  $70^\circ - 75^\circ$  and shifts to higher latitudes faster than in the South. The continuous shift of the EUV brightness in high latitudes corresponds to the zonal migrating flows (Howe *et al.*, 2011, 2013).

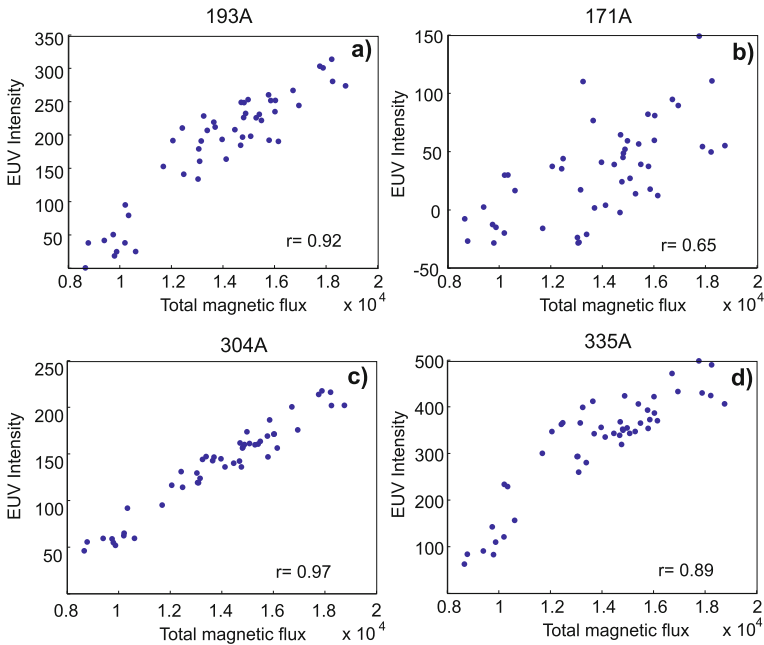


**Figure 4** Scatter plots of the integrated magnetic flux and the EUV intensities: (a) EUV 193 Å; (b) EUV 171 Å; (c) EUV 304 Å; (d) EUV 335 Å; the correlation coefficients are marked by “ $r$ ”. The EUV intensity is presented in normalized values.

#### 4. Discussion

We have presented the synoptic structure of Solar Cycle 24 during its ascending phase in the lines of Fe IX (171 Å), Fe XII and XXIV (193 Å), Fe XIV (211 Å), He II (304 Å), and Fe XVI (335 Å). The bright regions of the coronal maps show solar activity of various types. Each bright region from small to large scale coincides with strong magnetic flux (Figures 1a, b, c, d, e, and f). Large-scale magnetic structures such as coronal holes are seen in the 193 Å and 304 Å line maps. For example, in CR 2100 (Figure 1b) we see an extended coronal hole (longitudes 150°–200°). The He II synoptic maps reveal the chromospheric-network pattern and its evolution during the solar cycle. Therefore, such coronal synoptic maps provide information about coronal topology and its relationship with magnetic activity. The footpoints of coronal loops might be tracked using the 171 Å-line synoptic maps.

The synoptic structure of Solar Cycle 24 during the period 20 May 2010 to 31 August 2013 shows a relationship between emerging magnetic flux and emission in the 171 Å, 193 Å, 211 Å, 335 Å, and 304 Å maps, which corresponds to emission from the low corona, transition region, and chromosphere. The fluctuations in the emergence of magnetic flux (impulses of solar activity) are clearly seen in the sunspot-activity zones as intense regions in butterfly diagrams constructed from the coronal maps. The butterfly-shaped distribution of the brightness of the coronal maps and the magnetic-flux maps coincide and reveal the global structure of solar activity over the cycle. This structure is related to the internal pattern of the magnetic field generated by the action of the dynamo process. Understanding the nature of the internal rotation, meridional circulation, possible torsional oscillation, and convective motion are important for a full understanding of the solar cycle (Howard and

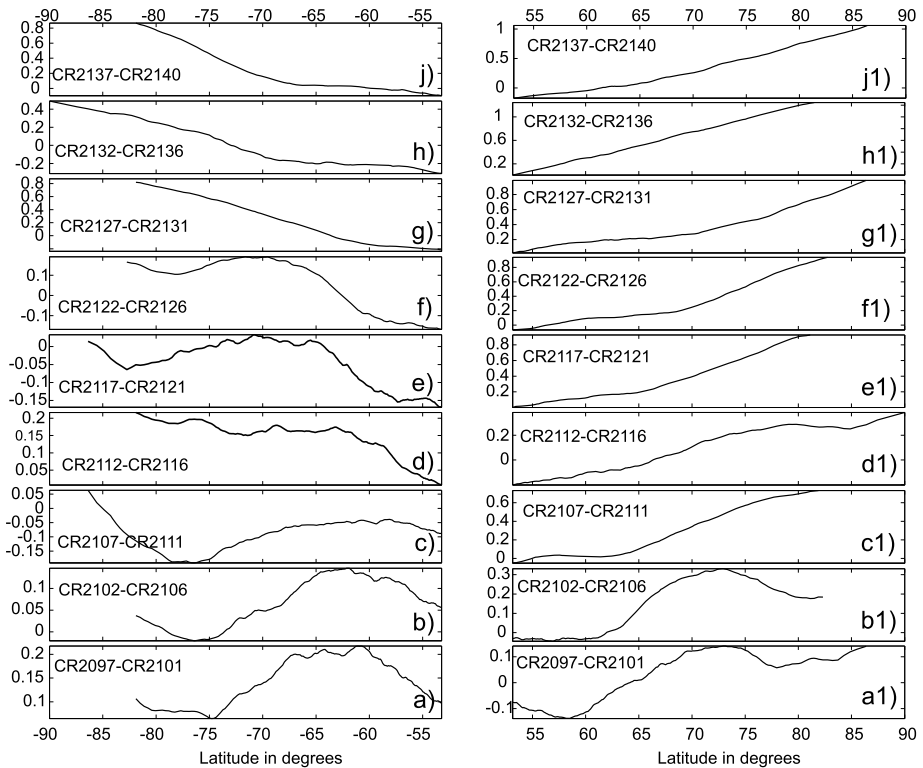


**Figure 5** The mean EUV intensity ( $171 \text{ \AA}$ ) as a function of latitude from  $53^\circ$  to  $90^\circ$  in northern (right panels) and southern (left panels) hemispheres, respectively, averaged over Carrington rotations: (a) CR 2097 – CR 2101 (20 May 2010 – 3 October 2010); (b) CR 2102 – CR 2106 (3 October 2010 – 16 February 2011); (c) CR 2107 – CR 2111 (16 February 2011 – 3 July 2011); (d) CR 2112 – CR 2116 (3 July 2011 – 16 November 2011); (e) CR 2117 – CR 2121 (16 November 2011 – 31 March 2012); (f) CR 2122 – CR 2126 (31 March 2012 – 15 August 2012); (g) CR 2127 – CR 2131 (15 August 2012 – 29 December 2012); (h) CR 2132 – CR 2136 (29 December 2012 – 15 May 2013); (j) CR 2137 – CR 2140 (15 May 2013 – 31 August 2013).

LaBonte, 1980; Ulrich and Boyden, 2005). These questions are all still unresolved and require further study. The recent analysis of SOHO/MDI, GONG, and SDO/HMI data (Howe *et al.*, 2011, 2013) revealed differences in the internal migrating zonal flow structure between Cycles 23 and 24. It was found that the high-latitude waves of higher solar rotation rate are well-defined during the ascending phase of Solar Cycle 23 but are only weakly visible in Cycle 24 (Howe *et al.*, 2011, 2013). Unfortunately, this analysis of global-mode frequencies is not sensitive to North–South asymmetries and therefore provides no information about any North–South asymmetry in the zonal flow structure. Nevertheless, the weak high-latitude branches of the migrating zonal flows in Cycle 24 may possibly be the cause of the observed weak high-latitude coronal activity waves that are associated with the large-scale magnetic-field structure on the Sun. However, we observed the strong relationship between the magnetic flux and the EUV brightness for low-latitude waves in the butterfly diagram (see Figures 2, 4).

The existence of the high- and low-latitude coronal waves is related to the dynamo. The low-latitude wave coincides with the sunspot distribution during the solar cycle. Now we



clearly see that high-latitude waves reflect the topology of the zonal flow inside the Sun (Howe *et al.*, 2011, 2013).

We emphasize that the high-latitude activity waves may be related to the extended solar cycle (Tappin and Altrock, 2013).

Thus, the observations of synoptic structure of Solar Cycle 24 in the photosphere, chromosphere, and corona demonstrate that the distribution of the emerging magnetic flux is crucial for the subsequent evolution and topology of the solar corona. The North–South asymmetry, impulses of solar activity, and any fluctuations of the tilt of the emerged magnetic flux make the cycle complicated and difficult to predict. However, it is obvious that the observed behavior of solar activity is closely related to the dynamo process that affects all levels within the Sun and its atmosphere: interior, photosphere, chromosphere, and corona. The delay of the polar magnetic-field reversals occurs because of the existence of strong surges of old polarity flux, which contribute to the polar magnetic field. These surges affect the coronal topology by weakening the high-latitude coronal-activity waves and make the waves difficult to observe. The nature of the impulses of solar activity in turn also require further study.

**Acknowledgements** Data courtesy of NASA/SDO and the AIA and HMI science teams. Thanks to Y. Ponyavin for help in preparing AIA data. We are grateful to P.H. Scherrer for useful comments.

## References

- Benevolenskaya, E.E., Kosovichev, A.G., Scherrer, P.H.: 2001, *Astrophys. J. Lett.* **554**, L107.
- Benevolenskaya, E.E., Kosovichev, A.G., Lemen, J.R., Slater, G.L., Scherrer, P.H.: 2002, *Astrophys. J. Lett.* **571**, L181.
- Dikpati, M., de Toma, G., Gilman, P.A.: 2006, *Geophys. Res. Lett.* **33**(5), L05102.
- Howard, R., LaBonte, B.J.: 1980, *Astrophys. J. Lett.* **239**, L33.
- Howe, R., Hill, F., Komm, R., Christensen-Dalsgaard, J., Komm, R., Larson, T.P., Schou, J., Thompson, M.J., Ulrich, R.: 2011, *J. Phys.* **CS-271**, 012074.
- Howe, R., Christensen-Dalsgaard, J., Hill, F., Komm, R., Larson, T.P., Schou, J., Thompson, M.J.: 2013, *Astrophys. J. Lett.* **767**, L20.
- Jiang, J., Cameron, R.H., Schmitt, D., Schussler, M.: 2013, *Space Sci. Rev.* **176**, 289. DOI.
- Lemen, J.R., Title, A.M., Akin, D.J., Boerner, P.F., Chou, C., Drake, J.F., Duncan, D.W., Edwards, C.G., Friedlaender, F.M., Heyman, G.F., Hurlburt, N.E., Katz, N.L., Kushner, G.D., Levay, M., Lindgren, R.W., Mathur, D.P., McFeaters, E.L., Mitchell, S., Rehse, R.A., Schrijver, C.J., Springer, L.A., Stern, R.A., Tarbell, T.D., Wuelser, J.-P., Wolfson, C.J., Yanari, C., Bookbinder, J.A., Cheimets, P.N., Caldwell, D., Deluca, E.E., Gates, R., Golub, L., Park, S., Podgorski, W.A., Bush, R.I., Scherrer, P.H., Gumminger, M.A., Smith, P., Auken, G., Jerram, P., Pool, P., Soufli, R., Windt, D.L., Beardsley, S., Clapp, M., Lang, J., Waltham, N.: 2012, *Solar Phys.* **275**, 17. DOI. ADS.
- Li, J., Jewitt, D., LaBonte, B.: 2000, *Astrophys. J. Lett.* **539**, L67. DOI. ADS.
- Pesnell, W.D.: 2012, *Solar Phys.* **281**, 507. DOI. ADS.
- Pesnell, W.D., Thompson, B.J., Chamberlin, P.C.: 2012, *Solar Phys.* **275**, 3. DOI. ADS.
- Petrie, G.J.D.: 2012, *Solar Phys.* **281**, 577. DOI. ADS.
- Scherrer, P.H., Bogart, R.S., Bush, R.I., Hoeksema, J.T., Kosovichev, A.G., Schou, J., Rosenberg, W., Springer, L., Tarbell, T.D., Title, A., Wolfson, C.J., Zayer, I. (MDI Engineering Team): 1995, *Solar Phys.* **162**, 129. DOI. ADS.
- Scherrer, P.H., Schou, J., Bush, R.I., Kosovichev, A.G., Bogart, R.S., Hoeksema, J.T., Liu, Y., Duvall, T.L., Zhao, J., Title, A.M., Schrijver, C.J., Tarbell, T.D., Tomczyk, S.: 2012, *Solar Phys.* **275**, 207. DOI. ADS.
- Shiota, D., Tsuneta, S., Shimojo, M., Sako, N., Orozco Suarez, D., Ishikawa, R.: 2012, *Astrophys. J.* **753**, 157.
- Spruit, H.C.: 2012, *Prog. Theor. Phys. Suppl.* **195**, 185.
- Svalgaard, L., Kamide, Y.: 2012, *Astrophys. J.* **763**, 6.
- Tappin, S.J., Altrock, R.C.: 2013, *Solar Phys.* **282**, 249. DOI. ADS.
- Ulrich, R.K., Boyden, J.E.: 2005, *Astrophys. J. Lett.* **620**, L123.
- Wang, Y.-M., Nash, A.G., Sheeley, N.R. Jr.: 1989, *Astrophys. J.* **347**, 529.